



Aeroacoustic Characteristic Analyses of Coaxial Rotors in Hover and Forward Flight

Bo Wang¹ · Chenkai Cao¹ · Qijun Zhao¹ · Xin Yuan¹ · Zheng Zhu¹

Received: 8 December 2020 / Revised: 26 May 2021 / Accepted: 24 June 2021 / Published online: 23 August 2021
© The Korean Society for Aeronautical & Space Sciences 2021

Abstract

A numerical method combining computational fluid dynamics (CFD) method and Ffowcs Williams–Hawkings (FW–H) equations is established for predicting acoustic characteristics of the coaxial rigid rotor in hovering and forward flight. The unsteady Reynolds-averaged Navier–Stokes (URANS) solver coupled with the moving-embedded grid technique is established to obtain sound source information in the flowfield with high accuracy. On the basis of the accurate solution for the coaxial rotor flowfield, the blade–vortex interaction (BVI) noise in hovering state and the high-speed impulsive (HSI) noise in high-speed forward flight are estimated by the Farassat 1A formula and the FW–H equation with a penetrable data surface (FW–H_{pds}), respectively. Then the sound pressure distribution characteristics and sound radiation pattern for the coaxial rotor in a hovering state and in a forward flight are obtained through the comparative analysis of the sound pressure time histories and the distribution of sound pressure levels of the upper rotor, lower rotor, and coaxial rotor. The simulation results indicate that significant unsteady characteristics appear in blade aerodynamic loading due to the Venturi effect, blade–vortex interaction phenomenon, and action of the downwash existing in the coaxial rotor flowfield, causing the loading noise of the coaxial rotor to occupy the dominant position in hovering state; the counter-rotating characteristics of the upper and lower rotors cause a significant phase difference between their respective sound pressure waveforms, and the phase difference is determined by the angle between the observation point and the intersection position of the upper and lower blades; the difference with the single rotor in terms of the severe HSI noise generated in the high-speed forward flight is that the noise radiation intensity of the coaxial rotor along both sides in the forward direction exhibits an approximately symmetrical distribution.

Keywords Helicopter · Rigid coaxial rotor · Aerodynamic noise · Navier–Stokes equation · Farassat 1A formula · FW–H_{pds} equation

1 Introduction

Helicopters have characteristics such as hovering, loitering, vertical takeoff and landing that fixed-wing aircraft cannot match. However, the conventional single-rotor helicopter with a tail rotor configuration cannot achieve high-speed flight due to existing limiting factors such as advancing blade shock and retreating blade stall. This shortcoming limits the application of helicopters, as it is challenging for a low-speed helicopter to meet the speed requirements of emergency rescue, material transportation, and criminal

investigation, pursuit, and capture. Therefore, research of a new configuration for a helicopter with high-speed flight capability has a significant meaning for broadening the application prospects of helicopters in the military and civilian fields and is currently an important direction of helicopter development.

At present, the high-speed helicopters in the world primarily have two popular configurations—the tilt-rotor aircraft and the rigid coaxial rotor helicopter. Through the counter-rotation of the two rotors, the anti-torque is mutually canceled out in the coaxial rotor helicopter, removing the tail rotor used to balance the anti-torque and improving the power utilization efficiency. Moreover, this configuration gives full play to the lift potential of the advancing blades by offloading the retreating blades and reducing rotor rotating speed, breaking through the aerodynamic constraints of the rotors for a conventionally configured helicopter during high-speed flight. That means the

✉ Bo Wang
wangbo@nuaa.edu.cn

¹ National Key Laboratory of Rotorcraft Aeromechanics, College of Aerospace Engineering, Nanjing University of Aeronautics and Astronautics, Nanjing 210016, China

rigid coaxial rotor helicopters have high-speed flight capabilities. In terms of the problems that arise with manipulating a tilt-rotor aircraft in a transition state, the rigid coaxial rotor helicopter has more stable high-speed forward flight characteristics and has become the latest research hotspot in the recent international high-speed helicopter field.

The coaxial rotor helicopter has great advantages in practical application. However, the unique configuration and operating mode of the coaxial rotor make its aerodynamic environment more complex than that of the conventional single rotor. Due to the counter-rotation of the upper and lower rotors, not only does interaction occur in the flowfield between the upper rotor blade-tip vortex and the lower rotor blade, but the upper rotor blade-tip vortex and the lower rotor blade-tip vortex also interact with each other. The complex interaction phenomenon has a serious impact on the motion of the blade-tip vortex, thereby generating severe blade–vortex interaction (BVI) noise. When the helicopter is in high-speed forward flight, the tip Mach number of advancing blade reaches transonic velocity; simultaneously, the delocalization phenomenon occurs, generating intense high-speed impulse (HSI) noise. Therefore, noise prediction and noise characteristic analysis of the coaxial rotor is an important issue in the field of technological research for that configuration. However, the complex aerodynamic environment poses a challenge to simulate the aerodynamic noise of the coaxial rotor. Unlike the quasi-steady flowfield characteristics of the conventional rotor in a hovering state, severe BVI and vortex–vortex interaction phenomena arise in the flowfield of the coaxial rotor, the motion of the blade-tip vortex is complex, and an asymmetrical distribution appears in the induced downwash; these characteristics cause significant unsteady characteristics to also appear even in a hovering state. In addition, during high-speed forward flight, the strong compression of the advancing blades and the large reverse flow region of the retreating blades cause a significant airflow separation phenomenon on the blade surface. These phenomena pose considerable challenges to the flowfield simulation, noise prediction, and noise characteristic analysis of the rigid coaxial rotor.

Some researches were conducted to investigate the aerodynamic and acoustic characteristics of the coaxial rotor. Leishman developed a blade element momentum theory suitable for the simulation of the coaxial rotor flow field [1]. Andrew [2] and Bagai [3] studied the aerodynamic characteristics of the coaxial rotor by the free wake vortex model. Kim [4] developed a vortex transport model suitable for the coaxial rotor. Tong [5] et al. introduced the momentum source term in the computational fluid dynamics (CFD) method to simulate the action of the coaxial rotor blades on the flowfield. Although the computational speeds of these methods are fast, they are less likely to accurately obtain the unsteady airload on the blade surface. Lakshminarayan [6] combined the sliding

grid and the embedded grid methods, while Xu [7] and Ye [8] numerically simulated the flowfield and aerodynamic characteristics of the coaxial rotor through a CFD method based on the unstructured grid, obtaining the detailed features of flowfield, but the acoustics characteristics of coaxial rotors were not involved. Further studies on the noise characteristics of the coaxial rotor were conducted by Wachspress [9] based on the vortex filament theory and the WOPWOP program and by Kim [10, 11] based on the vortex transport model and the Farassat 1A formula. Detailed acoustic analyses were conducted by Jia [12, 13] to evaluate the relative importance between blade-crossover interactions and self-BVIs at various forward flight speeds using CFD/computational structural dynamics loose-coupling simulations. In summary, current research on the coaxial rotor focuses mainly on flowfield prediction and aerodynamic characteristics analysis. Fewer studies exist on noise calculation and noise characteristics analysis. It is valuable to conduct the aeroacoustic characteristics analyses of coaxial rotors in different flight conditions using higher accuracy CFD method coupled with FW–H equations.

In this paper, the unsteady flowfield of coaxial rotors has been simulated by solving the compressible Reynolds-averaged Navier–Stokes (RANS) equation based on the moving-embedded grid technique, the dual-time method, the Spalart–Allmaras model, and the high-precision Riemann–Muskhelishvili (R-MUSCL) scheme, thus the accurate noise source information can be obtained. Then, the numerical method for predicting the aerodynamic noise of the coaxial rotor is established. The BVI noise in hovering flight and HSI noise in forward flight are evaluated respectively using the Farassat 1A formula and FW–H equation with a penetrable data surface. On this basis, detailed analyses are conducted on the sound pressure time histories, spectral characteristics, and radiation characteristics of the aerodynamic noise for the coaxial rotor in hovering and forward flight states, and meaningful conclusions are obtained.

2 Numerical Method

2.1 CFD Method

The unsteady flowfield of the coaxial rotor is predicted by CFD method based on the RANS solver CLORNS [14]. The governing equations for predicting the flowfield of the coaxial rotor are written in finite-volume forms as

$$\frac{\partial}{\partial t} \iiint_V \mathbf{W} dV + \iint_S \mathbf{F} dS = \iint_S \mathbf{F}_v dS, \quad (1)$$

where \mathbf{W} is the vector of conservative variables, \mathbf{F} is the convective flux, and \mathbf{F}_v is the viscous flux, which can be written as

$$\mathbf{W} = \begin{bmatrix} \rho \\ \rho u \\ \rho v \\ \rho w \\ \rho E \end{bmatrix}, \quad \mathbf{F} = \begin{bmatrix} \rho(q_n - q_b) \\ \rho u(q_n - q_b) + n_x p \\ \rho v(q_n - q_b) + n_y p \\ \rho w(q_n - q_b) + n_z p \\ \rho H(q_n - q_b) + q_b p \end{bmatrix}, \quad \mathbf{F}_v = \begin{bmatrix} 0 \\ n_x \tau_{xx} + n_y \tau_{xy} + n_z \tau_{xz} \\ n_x \tau_{yx} + n_y \tau_{yy} + n_z \tau_{yz} \\ n_x \tau_{zx} + n_y \tau_{zy} + n_z \tau_{zz} \\ n_x \Phi_x + n_y \Phi_y + n_z \Phi_z \end{bmatrix} \tag{2}$$

where t is the physical time, V is the control cell volume and S is the surface of the control cell. $\mathbf{n} = [n_x \ n_y \ n_z]^T$ is the local surface normal vector. u, v, w are the components of fluid velocity vector. q_n is the normal velocity of fluid, and q_b is the normal velocity of blade grid. E, H, p and ρ are total energy, total enthalpy, pressure and density. τ is viscous force and Φ is viscous convection term. The viscosity coefficients are calculated by the Spalart–Allmaras turbulence model [15]. The nonslip boundary condition is adopted for blade surfaces and the non-reflecting condition is adopted for the outermost boundary of both blade grids and background grids. To improve the efficiency of solving the flowfield, the implicit LU-SGS format is used for the dual time-stepping method [16]. A finite-volume method is used for spatial discretization. The three-order ROE-MUSCL scheme and central difference scheme are applied to calculate inviscid flux and viscid flux, respectively. To avoid the non-physical solutions that may be generated in the Roe format, Harten’s entropy correction is applied.

A single grid cannot achieve the counter-rotation of the upper and lower rotor, thus the moving-embedded grid method is used in this study. Figure 1 gives the schematic of the moving-embedded grid system. The blade grids have $197 \times 30 \times 65$ points and the distance from the outer boundary to the blade surface is $1.3c$, where c is the chord length. The background grids have $249 \times 130 \times 210$ points, and the size is $4L \times 5L \times 4L$, where L is the aspect ratio. The local grids located at the rotor plane and blade-tip are refined. The processes of grid generation and CFD flowfield simulation

are completed in the Intel Visual Fortran compiler. The detailed features of the unsteady flowfield of coaxial rotors can be obtained by the CFD method, and then be used as the noise source information for acoustics calculation.

When setting the outer boundary of the blade grid, the problem of crossover occurs between the blade and other blade grids in the course of the counter-rotation of the upper and lower rotors should be avoided, thereby avoiding the adverse effects that may be generated during the flowfield information exchange in the moving-embedded grid method. Hole-map method is simplified in the vertical direction to augment the efficacy of identifying the hole cells and hole boundary in Cartesian background grids. Thus, the hole cells can be re-recognized and marked when azimuth updating is performed. On the other hand, the inverse map is established in a similar algorithm, and PSSDE (pseudo-searching scheme of donor elements) is used for donor element searching [14, 17].

2.2 Trim Model

The Newton–Raphson method is adopted to determine the blade collective, lateral cyclic, and longitudinal cyclic pitch angles for each rotor under specific conditions. By trimming solution [18], the upper and lower rotors are torque balanced and achieve the target thrust coefficient, rolling and pitching moments. The blade pitch θ of each rotor for the coaxial system at azimuth ψ are expressed as follows:

$$\begin{aligned} \theta_U &= \theta_{0U} + \theta_{1cU} \cos \psi_U + \theta_{1sU} \sin \psi_U, \\ \theta_L &= \theta_{0L} + \theta_{1cL} \cos \psi_L + \theta_{1sL} \sin \psi_L. \end{aligned} \tag{3}$$

The rotor control input vector and the response vector in the trimming procedure are respectively given by

$$\begin{aligned} X &= \{\theta_{0U}, \theta_{1sU}, \theta_{1cU}, \theta_{0L}, \theta_{1sL}, \theta_{1cL}\}, \\ Y &= \{\sum C_T, \sum C_Q, LOS, C_{MzU}, \sum C_{Mx}, C_{MzL}\}, \end{aligned} \tag{4}$$

where C_T and C_Q represent the thrust coefficient and torque coefficient of the coaxial system, LOS, C_{Mz} and C_{Mx} represent the lift offset, pitching moment coefficient and rolling moment coefficient, respectively. Subscripts U and L represent the upper rotor and lower rotor respectively.

$$\begin{aligned} \sum C_T &= C_{TU} + C_{TL}, \quad \sum C_Q = C_{QU} + C_{QL}, \\ \sum C_{Mx} &= C_{MxU} + C_{MxL}, \quad LOS = \frac{|C_{MxU}| + |C_{MxL}|}{\sum C_T \cdot R}. \end{aligned} \tag{5}$$

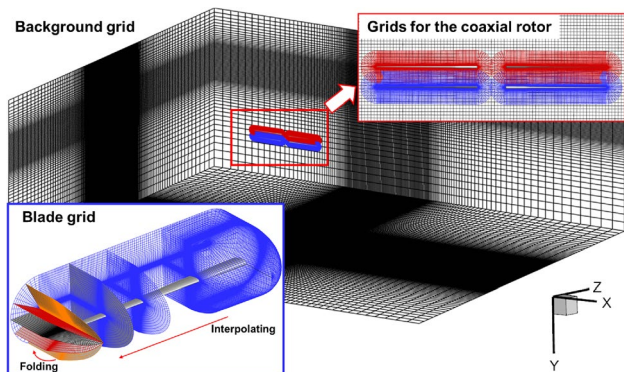


Fig. 1 Schematic of the moving-embedded grid system

Then the equation to solve is

$$Y(X) - Y^{\text{target}} = 0, \tag{6}$$

$$X^{(n+1)} = X^{(n)} - J^{-1}(Y^{(n)} - Y^{\text{target}}), \tag{7}$$

$$J = \begin{bmatrix} \frac{\partial \sum C_T}{\partial \theta_{0U}} & \frac{\partial \sum C_T}{\partial \theta_{1sU}} & \frac{\partial \sum C_T}{\partial \theta_{1cU}} & \frac{\partial \sum C_T}{\partial \theta_{0L}} & \frac{\partial \sum C_T}{\partial \theta_{1sL}} & \frac{\partial \sum C_T}{\partial \theta_{1cL}} \\ \frac{\partial \sum C_Q}{\partial \theta_{0U}} & \frac{\partial \sum C_Q}{\partial \theta_{1sU}} & \frac{\partial \sum C_Q}{\partial \theta_{1cU}} & \frac{\partial \sum C_Q}{\partial \theta_{0L}} & \frac{\partial \sum C_Q}{\partial \theta_{1sL}} & \frac{\partial \sum C_Q}{\partial \theta_{1cL}} \\ \frac{\partial \theta_{0U}}{\partial LOS} & \frac{\partial \theta_{1sU}}{\partial LOS} & \frac{\partial \theta_{1cU}}{\partial LOS} & \frac{\partial \theta_{0L}}{\partial LOS} & \frac{\partial \theta_{1sL}}{\partial LOS} & \frac{\partial \theta_{1cL}}{\partial LOS} \\ \frac{\partial C_{MzU}}{\partial C_{MzU}} & \frac{\partial C_{MzU}}{\partial C_{MzU}} & \frac{\partial C_{MzU}}{\partial C_{MzU}} & \frac{\partial C_{MzU}}{\partial C_{MzU}} & \frac{\partial C_{MzU}}{\partial C_{MzU}} & \frac{\partial C_{MzU}}{\partial C_{MzU}} \\ \frac{\partial \theta_{0U}}{\partial \sum C_{Mx}} & \frac{\partial \theta_{1sU}}{\partial \sum C_{Mx}} & \frac{\partial \theta_{1cU}}{\partial \sum C_{Mx}} & \frac{\partial \theta_{0L}}{\partial \sum C_{Mx}} & \frac{\partial \theta_{1sL}}{\partial \sum C_{Mx}} & \frac{\partial \theta_{1cL}}{\partial \sum C_{Mx}} \\ \frac{\partial \theta_{0U}}{\partial C_{MzL}} & \frac{\partial \theta_{1sU}}{\partial C_{MzL}} & \frac{\partial \theta_{1cU}}{\partial C_{MzL}} & \frac{\partial \theta_{0L}}{\partial C_{MzL}} & \frac{\partial \theta_{1sL}}{\partial C_{MzL}} & \frac{\partial \theta_{1cL}}{\partial C_{MzL}} \\ \frac{\partial \theta_{0U}}{\partial \theta_{1sU}} & \frac{\partial \theta_{1cU}}{\partial \theta_{1sU}} & \frac{\partial \theta_{0L}}{\partial \theta_{1sL}} & \frac{\partial \theta_{1cL}}{\partial \theta_{1sL}} \end{bmatrix}, \tag{8}$$

where $Y^{\text{target}} = \{\sum C_T^{\text{target}}, 0, LOS^{\text{target}}, 0, 0, 0\}$, and J is the Jacobian matrix.

The trimming of hovering rotor is similar to the forward case, while is simpler with only two inputs θ_U, θ_L and two outputs $\sum C_T, \sum C_Q$.

2.3 Acoustic Analogy Method

In terms of the methods for predicting the aerodynamic noise, Ffowcs Williams and Hawkins developed the FW–H equation based on the Lighthill acoustic analogy method; the effect of moving solid boundaries on fluid action was taken into account for the first time. Farassat et al. put forward the solution formula (Farassat 1A) for FW–H equations in the time domain. The formulation Farassat 1A [19] can be written as

$$p' = p'_T + p'_L, \tag{9}$$

$$4\pi p'_T = \int \left[\frac{\rho_0(\dot{\mathbf{U}} \cdot \hat{\mathbf{n}} + \mathbf{U} \cdot \dot{\hat{\mathbf{n}}})}{r(1 - \mathbf{M} \cdot \hat{\mathbf{r}})^2} \right]_{\text{ret}} ds + \int \left[\frac{\rho_0 \mathbf{U} \cdot \hat{\mathbf{n}}(r\dot{\mathbf{M}} \cdot \hat{\mathbf{r}} + a_0(\mathbf{M} \cdot \hat{\mathbf{r}} - \mathbf{M} \cdot \mathbf{M}))}{r^2(1 - \mathbf{M} \cdot \hat{\mathbf{r}})^3} \right]_{\text{ret}} ds, \tag{10}$$

$$4\pi p'_L = \frac{1}{a_0} \int \left[\frac{\mathbf{L} \cdot \hat{\mathbf{r}}}{r(1 - \mathbf{M} \cdot \hat{\mathbf{r}})^2} \right]_{\text{ret}} ds + \int \left[\frac{\mathbf{L} \cdot \hat{\mathbf{r}} - \mathbf{L} \cdot \mathbf{M}}{r(1 - \mathbf{M} \cdot \hat{\mathbf{r}})^2} \right]_{\text{ret}} ds + \frac{1}{a_0} \int \left[\frac{\mathbf{L} \cdot \hat{\mathbf{r}}(r\dot{\mathbf{M}} \cdot \hat{\mathbf{r}} + a_0(\mathbf{M} \cdot \hat{\mathbf{r}} - \mathbf{M} \cdot \mathbf{M}))}{r^2(1 - \mathbf{M} \cdot \hat{\mathbf{r}})^3} \right]_{\text{ret}} ds, \tag{11}$$

where p'_L is the total sound pressure, p'_T is the thickness sound pressure, p'_L is the loading sound pressure. a_0 and ρ_0 is the speed and density of sound in the undisturbed medium. The superscript “ \cdot ” means derivative of time. The subscript “ret” means the quantity evaluated at retarded time. $\hat{\mathbf{r}}$ is the unit vector in the radiation direction, $\hat{\mathbf{n}}$ is the unit outward normal vector to surface, \mathbf{M} is the local Mach number vector of source. r is the distance between observer and source, s is the surface of the acoustic source integration. \mathbf{U} is the local velocity vector of source surface. $\mathbf{L} = l \cdot \hat{\mathbf{n}}$, where l is the load of source surface.

The Farassat 1A formula can conveniently differentiate the thickness noise and the loading noise, attaining great success in predicting subsonic rotor noise. However, restricted by the challenges in calculating the volume integral, one cannot use the Farassat 1A formula to calculate transonic rotor noise (including quadrupole noise). In 1997, di Francescantonio extended Kirchhoff’s method by relaxing the restriction on the selection of the motion control plane for the FW–H equation, used a penetrable integral surface in place of a solid integral surface to re-derive the FW–H equation, and obtained a new method suitable for calculating the transonic rotor noise: the FW–H_{pds} method. The FW–H_{pds} equation [20] is particularly useful because it can be utilized directly to write an integral representation of the solution known as formula1A.

$$p' = p'_T + p'_L + p'_Q. \tag{12}$$

In the formula,

$$\begin{cases} 4\pi p'_T(\mathbf{x}, t) = \int_{f=0} \left[\frac{\rho_0(\dot{U}_n + U_n)}{r(1 - M_r)^2} \right]_{\text{ret}} ds + \int_{f=0} \left[\frac{\rho_0 U_n(r\dot{M}_r + a_0(M_r - M^2))}{r^2(1 - M_r)^3} \right]_{\text{ret}} ds \\ 4\pi p'_L(\mathbf{x}, t) = \frac{1}{a_0} \int_{f=0} \left[\frac{\dot{L}_r}{r(1 - M_r)^2} \right]_{\text{ret}} ds + \int_{f=0} \left[\frac{L_r - L_M}{r^2(1 - M_r)^2} \right]_{\text{ret}} ds + \frac{1}{a_0} \int_{f=0} \left[\frac{L_r(r\dot{M}_r + a_0(M_r - M^2))}{r^2(1 - M_r)^3} \right]_{\text{ret}} ds \end{cases}, \tag{13}$$

where

$$U_i = [1 - (\rho/\rho_0)]v_i + (\rho u_i/\rho_0), \tag{14}$$

$$L_i = P_{ij}n_j + \rho u_i(u_n - v_n), \tag{15}$$

where the dots on \dot{L}_r , \dot{U}_n , and \dot{M}_r denote the rate of variation with respect to source time. $L_M = L_i M_i$, and a subscript r or n indicates a dot product of the vector with the unit vector in the radiation direction \hat{r} or the unit vector in the surface normal direction \hat{n} , respectively.

When the selected integral surface contains nonlinear flow, p'_T , p'_L , and p'_Q in the aforementioned formula lose physical meaning and retain only mathematical meaning; however, at this time, the contribution of the quadrupole noise caused by the nonlinear flow is reflected in the first two surface integral terms, the third term p'_Q is approximately zero, and the sum of the first two terms is the total rotor noise. Therefore, the FW-H_{pds} method can be used to calculate the transonic rotor noise generated under high-speed forward flight. In contrast to the Kirchhoff method, which can similarly be used to estimate the transonic rotor noise, the FW-H_{pds} method is established in both linear and nonlinear regions and is more robust. Moreover, the Kirchhoff method has strict requirements on the selection of the integral surface locations. The integral surface must be located in the far-field linear region, thus, it is unable to estimate the near-field noise. Therefore, the FW-H_{pds} method is selected to study the noise characteristics of the coaxial rotor in high-speed forward flight. The grid surface surrounding the blade is selected as the integral surface of the sound source, thus the pressure data extracted from the N-S solution is used as the FW-H_{pds} surface data without interpolation, avoiding the loss in precision caused by interpolation.

In hovering flight, the rotor aerodynamic noise is composed mainly of the thickness noise and the loading noise; therefore, the Farassat 1A formula is used in this study when calculating the aerodynamic noise of the coaxial rotor in hovering flight. In high-speed forward flight, HSI noise-dominant aerodynamic rotor noise. Therefore, the FW-H_{pds} method is used to calculate transonic noise.

2.4 Validation of the Calculation Method

The Harrington Rotor-2 is used to validate the accuracy of the established CFD method for predicting the flowfield of the coaxial rigid rotor in hovering flight. Besides, the Harrington Rotor-1 single system (HS1) and coaxial system (HC1) are used to validate the computational predictions of the CFD solver in forward flight [18]. The time-steps chosen in the paper corresponds to 1.0° of azimuth. The

sub-iteration number of LUSGS is set as 30 and then the residual of density could be reduced by at least 1 order.

Figures 2, 3 show the comparisons of calculated aerodynamic performance with experimental data [18, 21], where C_T is the thrust coefficient, C_Q is the torque coefficient, μ is the advancing ratio. As can be seen, the predictions are in good agreement with the experimental data.

The reliability of the noise calculation method in this study is validated using experimental data on the aerodynamic noise of the single rotor. Figure 4 shows the comparison of the sound pressure between the calculated results

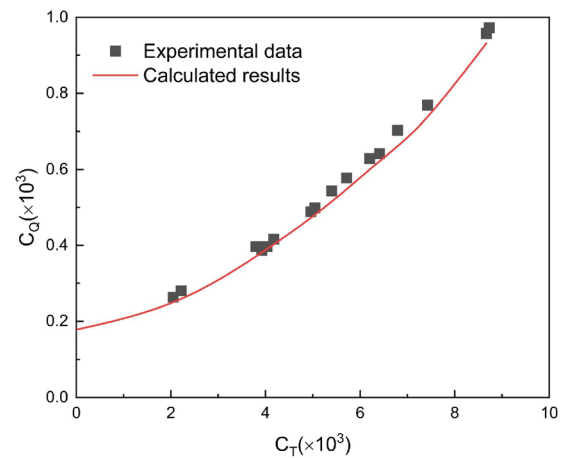


Fig. 2 Comparison of the calculated values and experimental data for the aerodynamic performance of the Harrington coaxial rotor-2 in hovering flight

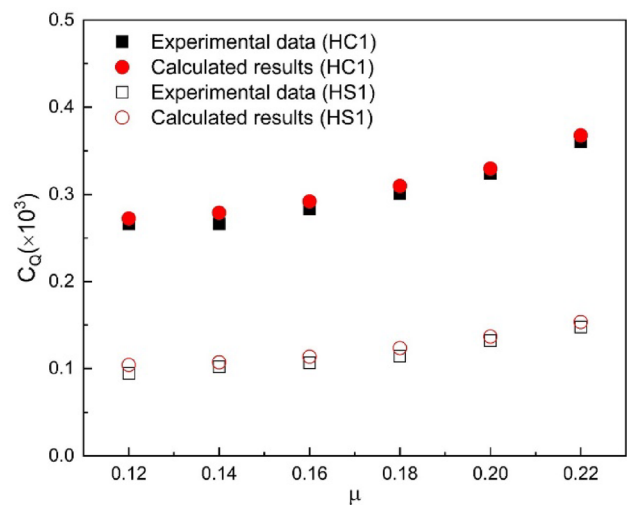


Fig. 3 Comparison of the numerical results and experimental data for the aerodynamic performance of the Harrington coaxial rotor-1 in forward flight

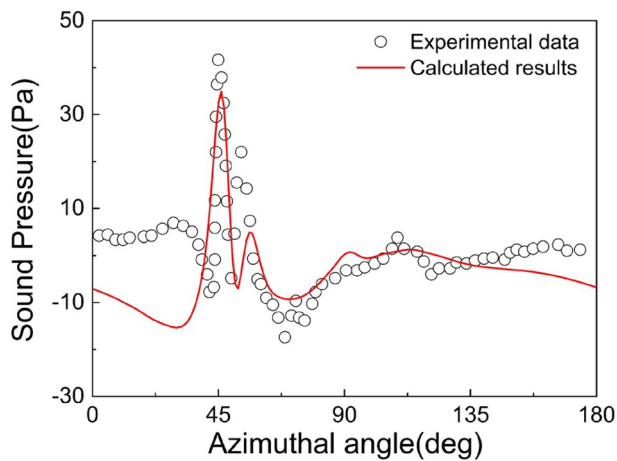


Fig. 4 Comparison of the sound pressure between the calculated result and experimental data for the AH-1/OLS rotor in descent flight

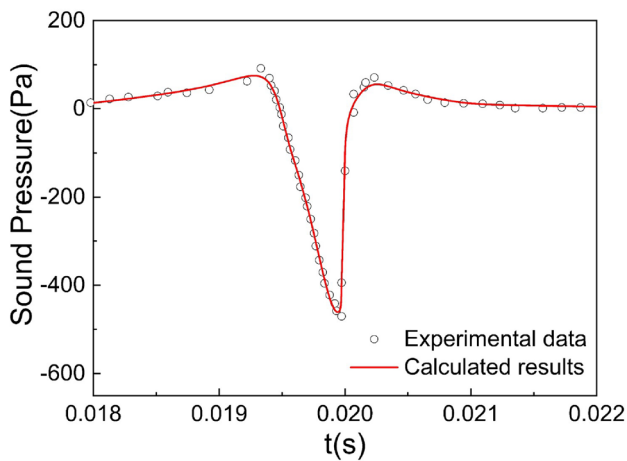


Fig. 5 Comparison of the sound pressure between the calculated result and experimental data for AH-1/OLS rotor in high-speed forward flight

and experimental data [22] for the AH-1/OLS model rotor in descent flight when the serious blade–vortex interaction phenomenon is generally observed. The advance ratio under this state was 0.164, the blade-tip Mach number was 0.664, and the backward tilt of the blade disk was 1°. The observation point was located at the lower front of the rotor, forming a 30° included angle with the rotor disk plane at a distance of 3.44 R from the center of rotation; this region suffers from more intense BVI noise radiation. The sound pressure signal in Fig. 4 has relatively strong impulse characteristics, which is a typical noise signal for BVI. Some deviations from the experimental values arise in the calculated peak values and in the sound pressure waveform. However, the goodness of fit between the calculation results in this study and the experimental values

is acceptable. Thus, the calculation method established in this paper can effectively predict the BVI noise.

Figure 5 compares the calculated sound pressure and experimental data [23] for the AH-1/OLS model rotor in high-speed forward flight. The advance ratio is 0.345, the blade-tip Mach number is 0.666, and the maximum Mach number of the advancing blade-tip reaches 0.896. The observation point is located directly in front of the rotor disk plane at a distance of 3.44 R from the center of rotation. The blade-tip is in transonic flow and generates severe HSI noise in this condition. It can be seen that the calculated sound pressure agrees well with the experimental data in terms of capturing both the negative peak of HSI noise and the pulse waveform. Thus, the calculation method established in this study can effectively predict the HSI noise.

3 Aerodynamic Noise Characteristics in Hovering Flight

The model coaxial rotor studied in this paper contains two two-bladed rotors; the upper rotor executed right-handed rotation, while the lower rotor executed left-handed rotation. The model rotor radius is 2.6 m with a chord of 0.2 m; thus, the blade aspect ratio is 13. The upper and lower rotors are spaced vertically at a distance of 0.15R, the cutoff position of the blade is 0.2R. The rotor blades have a linear twist of -10° and a standard rectangular tip, using a single NACA0012 airfoil. The blade-tip Mach numbers of the upper and lower rotor are both 0.556. In trim process, the target C_T is set as 0.013 for the coaxial rotor model in hover, and each rotor shares same half of total thrust. As a result, the pitches of upper and lower rotor blade in hovering flight are 13.80° and 14.75° respectively.

To facilitate subsequent analysis, four blades of the coaxial rotor are labeled. The two blades of the upper rotor are designated “U-1” (initial azimuth angle at 90°) and “U-2” (initial azimuth angle at 270°), and the two blades of the lower rotor are designated “L-1” (initial azimuth angle at

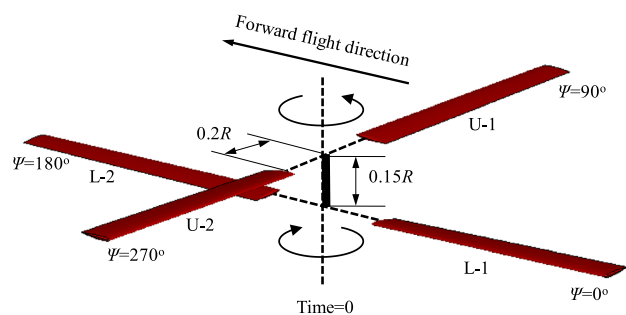


Fig. 6 Schematic of the calculation model for the coaxial rotor

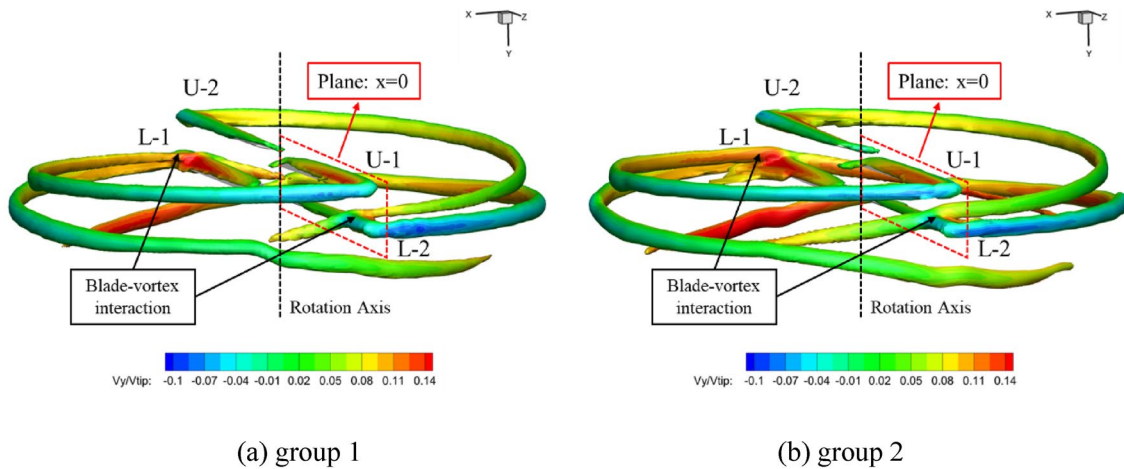


Fig. 7 The comparison of iso-surface of vorticity magnitude f between group 1 and group 2. ($\Psi_U = \Psi_L = 90^\circ$)

0°) and “L-2” (initial azimuth angle at 180°). Figure 6 shows the schematic of the calculation model for the coaxial rotor at the initial time.

3.1 Vortex Capturing Capability

The prediction accuracy of BVI noise in hovering state is greatly affected by the vortex capturing capability. To accurately capture the blade–vortex interaction, several groups of structured moving-embedded grids are generated to investigate the vortex capturing capability of the established CFD solver.

Figures 7, 8 present the comparison of iso-surface of vorticity magnitude and vorticity contour in a fixed plane for two different grids respectively. The blade grid used here is the same, which has $219 \times 70 \times 101$ points in the streamwise, normal direction and spanwise, respectively. Both two background grids have $257 \times 257 \times 198$ points in the two directions of horizon plane xoz and vertical direction. The difference is the background grid size in the area surrounding the blade tip, which is $0.1c$ (c is the chord

length) in group1 and $0.05c$ in group2. As can be seen, both two groups are able to capture the BVI interaction and the latter could capture more wake shape.

Although a further refined grid could improve the detail capturing ability, the size of group 2 grids is chosen for the numerical analyses in this paper, considering the computational cost.

3.2 Sound Pressure Time History

Figure 9 shows the positions of four typical observation points in the rotor disk plane. The distance between the center of rotation and the observation points is $5R$, where R is the radius of the rotor. Observation point #3 is located at the azimuth angle where the upper and lower blades meet, observation point #2 and observation point #4 are located

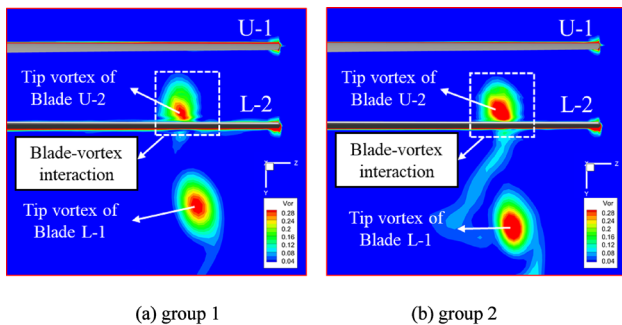


Fig. 8 Vorticity contours comparison in the plane ($x=0$)

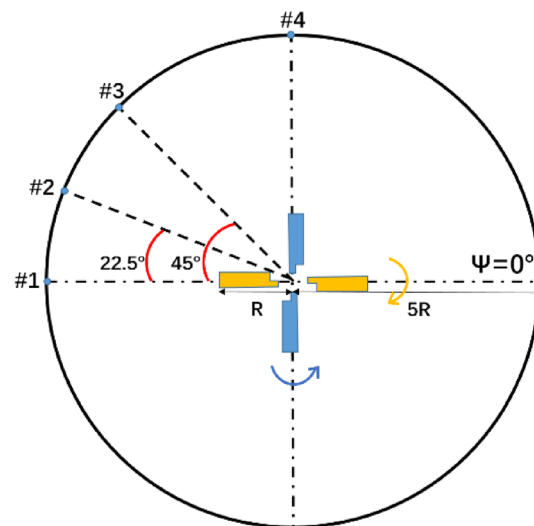


Fig. 9 Schematic of observer locations

in the rotor disk plane at the azimuthal angle of 157.5 deg and 90 deg respectively, and observation point #1 is located directly in front of the rotor.

To further explore the noise characteristics of the coaxial rotor, the sound pressures of the coaxial rotor and the single rotor are compared. Figure 10 shows the sound pressure time histories of a conventional single rotor at two typical positions (#1 and #3). In terms of a conventional single rotor, in the sound pressure time histories of different observation points at equal distances from the rotor axis within the same horizontal plane, although the positive or negative peak values appear at different azimuthal angles, the phase differences between adjacent peaks are the same, and the peaks appear the same number of times within a rotation period.

However, in terms of the coaxial rotor, the upper and lower rotors rotate in opposite directions, causing greater differences to arise in the peak values and in the phase difference at various observation positions. Figure 11, 12, 13, 14 show the sound pressure time histories of thickness, loading, and total noise separately generated by the coaxial rotor and the upper and lower rotor at different observation points. As a whole, the peak values of both upper and lower rotors appear twice in a rotation period, however, a significant

phase difference is observed between the waveforms generated by two rotors. For different observation points, the phase difference depends on the included angle between the observer location and the intersection of the upper and lower blades.

For observation point #3, which is just located at the azimuthal angle where the upper and lower blades meet, the phases of negative peak of the thickness sound pressure separately generated by upper and lower rotors are the same. And the phase at which the peak values of the total thickness sound pressure appear is the same as those for the upper and lower rotors alone, and the negative pressure peak value is greater than that at other observation positions. The sound pressure time history at observation point #3 shows similar characteristics as that of a single rotor with two blades. For observation point #1, the included angle between #1 and #3 is 45°, and the upper rotor lags behind the lower rotor by a 90° rotation to the #1 position; therefore, the phase difference occurring in the adjacent negative peak values is exactly 90°. For observation point #4, the included angle between #4 and #3 is 45°, and the lower rotor lags behind the upper rotor by a 90° rotation to the #4 position; therefore, the phase difference of adjacent negative peak values

Fig. 10 Sound pressure time history of the conventional single rotor

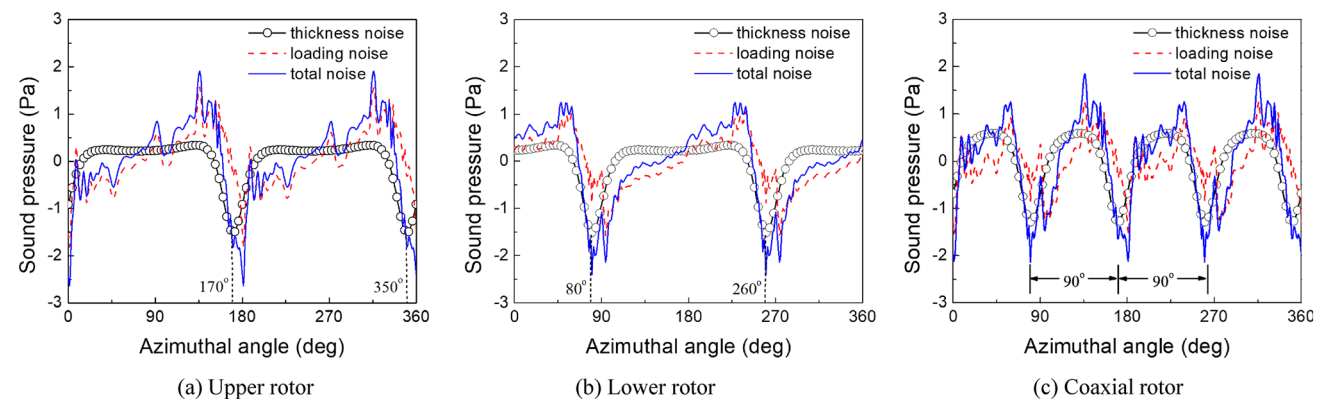
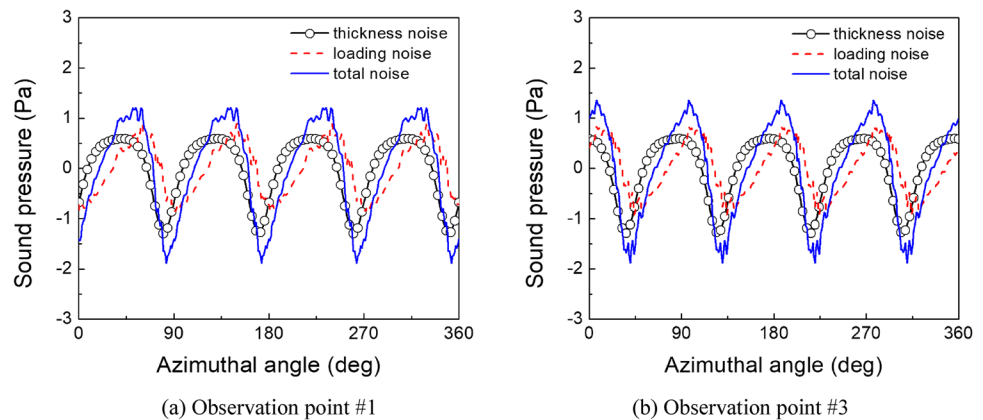


Fig. 11 Sound pressure time history of the coaxial rotor at observation point #1

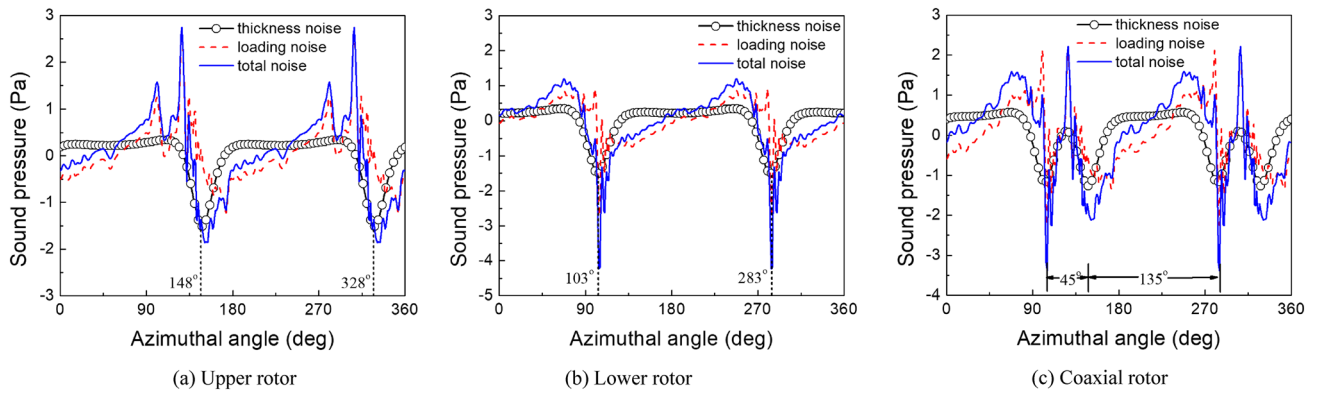


Fig. 12 Sound pressure time history of the coaxial rotor at observation point #2

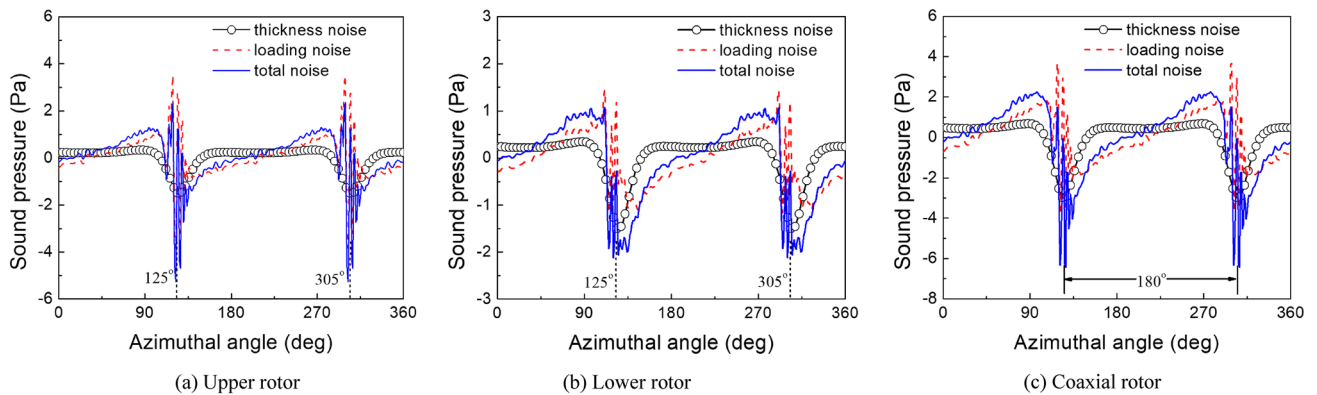


Fig. 13 Sound pressure time history of the coaxial rotor at observation point #3

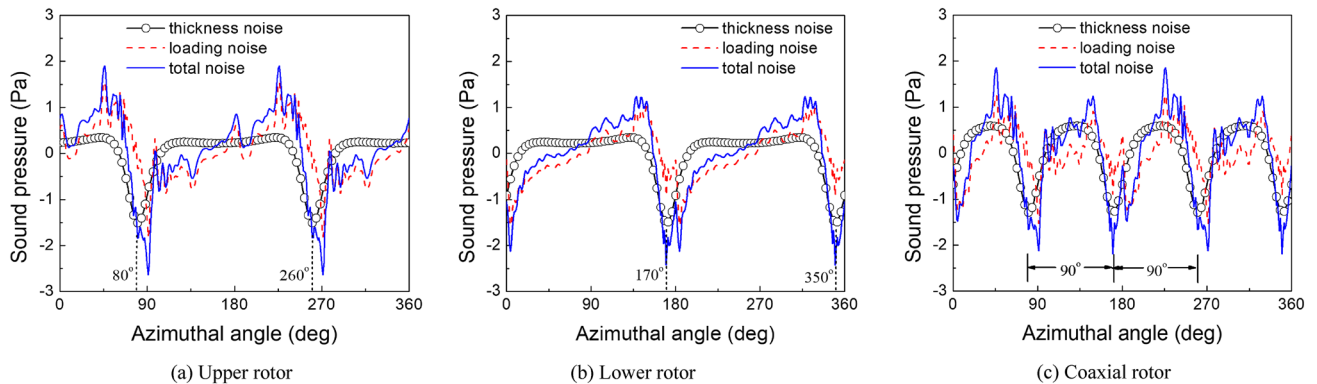


Fig. 14 Sound pressure time history of the coaxial rotor at Observation Point #4

is 90° . At #1 and #4, the waveforms are similar to that of the conventional four-bladed rotor. For observation point #2, the included angle between #2 and #3 is 22.5° , and the upper rotor lags behind the lower rotor by a 45° rotation to the #2 position; therefore, the phase difference of adjacent negative peak values is 45° .

In addition, by comparing the sound pressures of the upper and lower rotors at various observation positions, it can be seen that the negative peak values of the thickness noise are approximately the same; this similarity occurs because the blade shape and the blade-tip Mach numbers of the upper and lower rotor are the same and because the

thickness noise is determined mainly by the position and speed of the sound source on the blade surface and is unrelated to the relative motion of the two rotors.

However, significant differences arise in the sound pressure peak values of the loading noise generated by the upper and lower rotors. Compared with the gentle waveform of the thickness noise, the sound pressure signal of the loading noise oscillates more severely. The blade-tip vortex of the upper rotor causes severe aerodynamic interference on the blades of the lower rotor, generating complex BVI noise. Similarly, the downwash of the upper rotor causes periodic changes in the blade loading of the lower rotor. The severe changes in unsteady loading at the surface of the lower rotor blade increase the radiative intensity of the loading noise. In terms of the upper rotor, although the effect of the blade-tip vortex and downwash of the lower rotor on the upper rotor is limited, the Venturi effect phenomena still induce significant unsteady characteristics on the blade loading of the upper rotor, causing the loading noise of the upper rotor to also increase. In general, the loading noise of the upper rotor is greater than the loading noise of the lower rotor. A comparison of the calculation results for the single rotor noise given in Fig. 10 indicates that although the average thrust of the coaxial rotor and the single rotor is guaranteed to be the same under the current calculation state, the peak value of the loading noise of the single rotor is significantly smaller than that of the coaxial rotor, and the waveform is gentler. It is due to the smaller range of changes in the aerodynamic loading on the surface of a conventional single rotor blade.

3.3 Noise Radiation Characteristics

Figure 15a and b gives the spectrum frequency at observation points #1 and #3 (basic frequency BPF = 23.15 Hz), respectively; significant differences appear in the spectral characteristics at different positions within the plane.

Compared with the thickness noise at observation point #1, harmonic waves appear more times in the thickness noise at observation point #3 within the same frequency range. In general, the thickness noise is distributed predominantly in the low-frequency band; even in the current state of large thrust, the amplitude of the thickness noise in the low-frequency band remains close to that of the loading noise. However, as the frequency increases, the thickness noise decays rapidly. Therefore, in the middle-frequency and high-frequency bands, the amplitude of the loading noise is significantly higher than that of the thickness noise, and the loading noise is the main component of the total noise. In conclusion, the total noise is determined mainly by the thickness noise in the low-frequency band; as the frequency increases, the total noise is gradually dominated by the loading noise with the speed of attenuation slowing down or even increasing instead of decreasing.

To show the characteristics of noise radiation more clearly, the noise directivities of the coaxial rotor and the single rotor in the rotation plane are shown in Fig. 16. Observation points are located at a distance of $5R$ from the center of rotation. As shown in Fig. 16a, in terms of the conventional single rotor, the hovering state is similar to the quasi-steady state, the thickness noise and the loading noise both radiate outward evenly along the rotation plane of the rotor, and the radiation intensity is identical in different directions at the same distance. Therefore, the radiation pattern for the thickness noise, the loading noise, and the total noise of the single rotor shows a toroidal shape. However, greater differences appear in the characteristics of noise radiation between the coaxial rotor and the single rotor. Figure 16d indicates that the thickness noise and the loading noise of a coaxial rotor do not radiate evenly along the plane of the rotor but have significant directivity, with the most intense noise radiation at the four azimuth angles of 45° , 135° , 225° , and 315° ; these four azimuth angles are the azimuth angles where the upper and lower blades meet. This radiation characteristic is a unique characteristic for the hovering noise of the coaxial rotor. In addition, the thickness

Fig. 15 Spectral characteristics of coaxial rotor noise

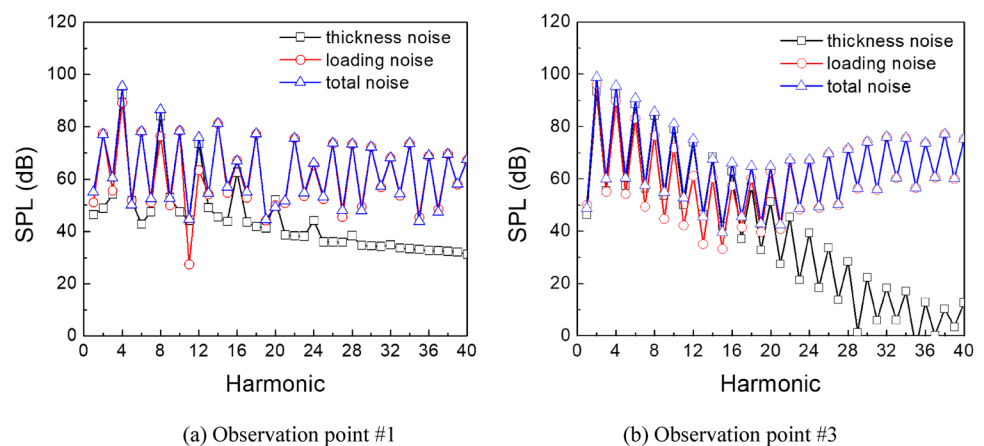
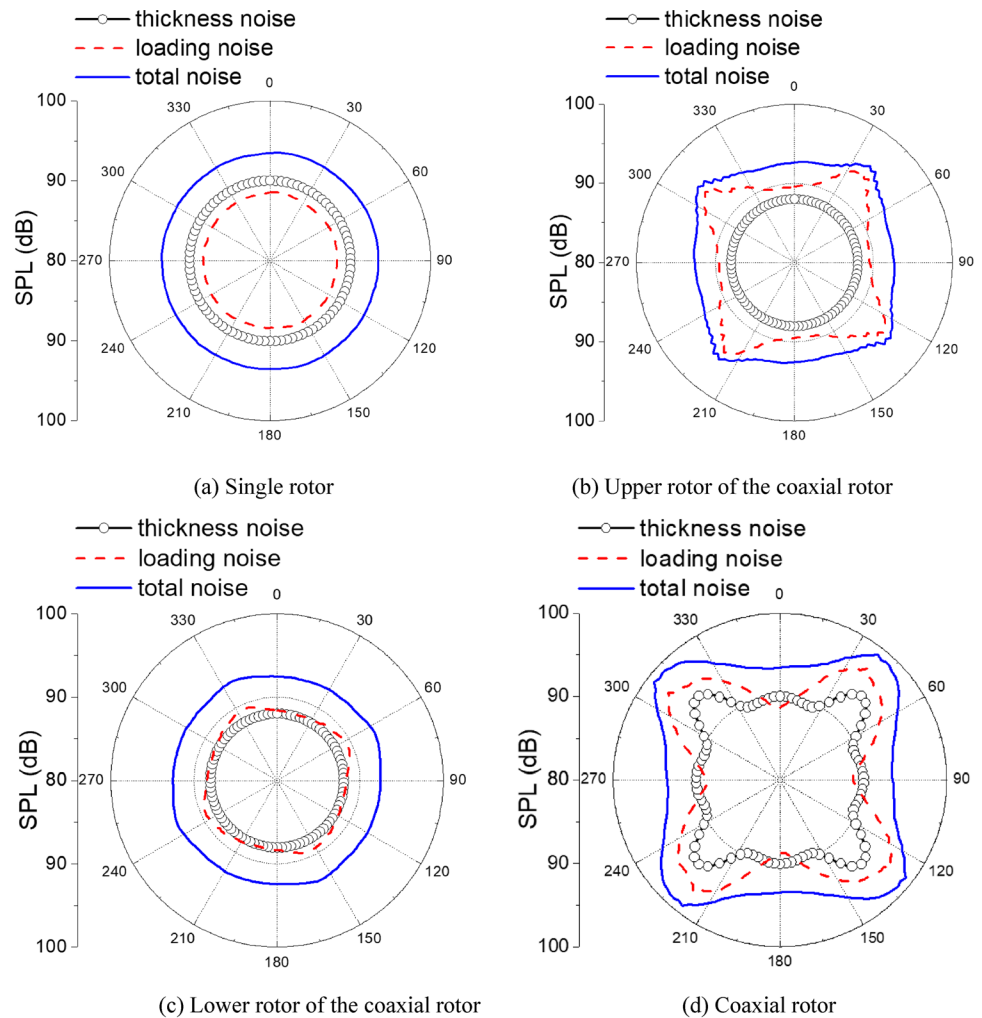


Fig. 16 Comparison of the noise propagation characteristics of the coaxial rotor and the single rotor



sound pressure level of the coaxial rotor may even be smaller than that of the conventional rotor in certain directions, which is due to the reversed direction of rotation for the upper and lower rotors of the coaxial rotor. This condition indirectly generates a result similar to the “modulated effect” of uneven blade spacing [24] and to a certain extent reduces the acoustic radiation intensity. By observing the loading noise level, one finds that in certain directions, the loading noise level of the coaxial rotor is close to that of the conventional rotor, and the loading noise increases significantly at the four azimuth angles where the upper and lower blades meet. A comparison of the loading noise of the upper and lower rotors in Fig. 16b and c indicates that the loading noise levels of the upper and lower rotors at the azimuth angles where the blades meet both increases obviously. The loading noise of the upper rotor is significantly greater than that of the lower rotor, and the loading noise directivity of the upper rotor is more significant than that of the lower rotor. Unlike the single rotor, the loading noises of the upper and lower rotors are both greater than their thickness noise; therefore, the loading noise is relatively large and dominates the total noise of the coaxial rotor.

4 Aerodynamic Noise Characteristics in Forward Flight

The model rotor adopted for the investigation of noise characteristics in forward flight is the same as the model rotor used in hover flight. To coordinate with the technique for a decrease in the rotational speed of the rotor during the high-speed forward flight, the blade-tip Mach number in forward flight drops 5% from the value of 0.556–0.528, that is, the rotational speed at the blade-tip is 179.55 m/s. The advance ratio is set as 0.6, and the corresponding forward flight speed is 388 km/h. In trim process, the target C_T is set as 0.013 for the coaxial rotor model in forward flight. Besides, upper and lower rotors are set to share the same thrust load, namely, $C_T/2$ and the lift offset is set as 0.35. As a result, the trimmed rotor pitches for forward flight are obtained, as shown in Table 1.

4.1 Sound Pressure Time History

Figure 17 shows the schematic of the positions of the observation points in the rotor disk plane. The distance of each

Table 1 Trimmed rotor pitches for forward flight

Parameter	θ_U/deg	θ_{L_s}/deg	θ_{L_c}/deg
Upper rotor	9.09	- 5.47	4.28
Lower rotor	8.95	- 4.53	4.48

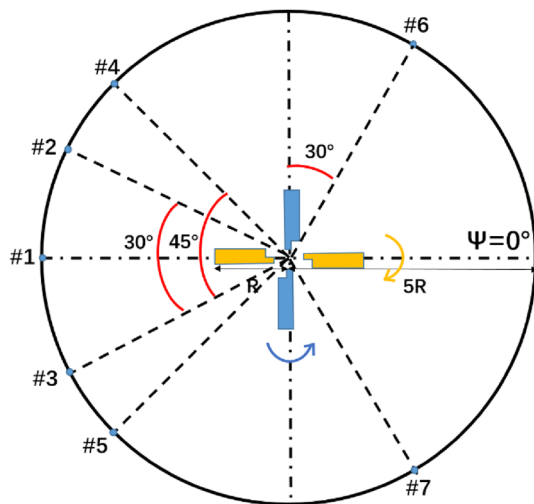


Fig. 17 Schematic of the positions of the observation points

observation point from the center of rotation is $5R$. Observation points #4 and #5 are at the azimuth angle where the upper and lower blades meet, observation point #1 is directly in front of the rotor, observation points #2, #3, #6 and #7 are located in the rotor disk plane with the azimuthal angle of 150° , 210° , 60° and 300° respectively.

Figure 18 shows the sound pressure time histories of the total noise and linear noise of the coaxial rotor at the observation points mentioned above. Observation points #6 and #7 are located rear of the rotor disk, and the rest of the observation points are located in front of the rotor disk. In the high-speed forward flight, the radiation of aerodynamic rotor noise is more intense towards the front. The noise directly in front of the rotor is more severe; in one rotation period, four large negative peak values appear in the sound pressure time history, which is similar to the HSI noise generated by the conventional single rotor with four blades. It is the result of the combined action of linear noise and nonlinear noise. However, no significant periodic peak values appear in the sound pressure waveforms of observation points located in the rear of rotor disk, and the sound pressure waveform fluctuates severely within a small range of amplitude disorderly and unsystematic.

The negative peak appearing four times in one rotation period for the observation points in front of the rotor is caused by each of the blades of the upper and lower rotors. The appearance time of the peak values changes with the

azimuthal angle of the position for the observation points. To gain insight into the contribution to the sound pressure of each blade at various azimuthal angles, the negative peak values corresponding to their blade are labeled, respectively, in Fig. 18a–e. In terms of observation point #1, which is located directly in front, the phase difference between adjacent peaks is 90° , and the peak values formed by the blades of the upper and lower rotors are similar in size while differ in appearance time. In the hovering state, the positions of the observation points where the phase positions of the sound pressure peaks generated by the upper and lower blades coincide are the locations where the upper and lower blades meet (observation points #4 and #5). However, the phase of the sound pressure peak values of the upper and lower blades do not coincide at observation points #4 and #5 in forward flight due to the existence of forward speed.

In the high-speed forward flight, the Mach numbers at the advancing blade tips of the upper and lower rotor are close to 0.9, and the advancing blade tips are both in transonic. The comparison of the sound pressure peak values of the rotational noise and the total noise in Fig. 18 indicates that the radiation of the quadrupole noise caused by the nonlinear phenomena is severe, the negative peak values of linear noise are far smaller than that of the total noise, so the HSI noise with quadrupole noise occupying the dominant position appears at this time. In addition, at the observation points in the rear of the rotor disk (#6 and #7), the sound pressure waveforms of the linear noise are relatively gentle, but the nonlinear noise sound pressure fluctuates severely.

4.2 Acoustic Radiation Characteristics

To further understand the acoustic radiation characteristics of the coaxial rotor in forward flight, Fig. 19a and b shows the noise directivity patterns in the horizontal plane and the vertical plane. The noise radiation characteristics of the upper, the lower, and the coaxial rotors in various directions can be clearly obtained. By observing the noise directivity patterns of the upper and lower rotors individually, it can be seen that the sound pressure levels of the observation points at the advancing side are greater. For example, the sound pressure levels of the upper rotor at observation point #2 (150°) and the lower rotor at observation point #3 (210°) are both greater than those at observation point #1 (180°). The sound pressure levels of the upper rotor at the observation points on the right side of the forward direction are greater than those of the lower rotor, and the sound pressure levels of the lower rotor at the observation points on the left side of the forward direction are greater than those of the upper rotor. This finding illustrates that the single rotor exhibits greater noise radiation intensity at the advancing side. It can be also found that the sound pressure levels at the observation points in

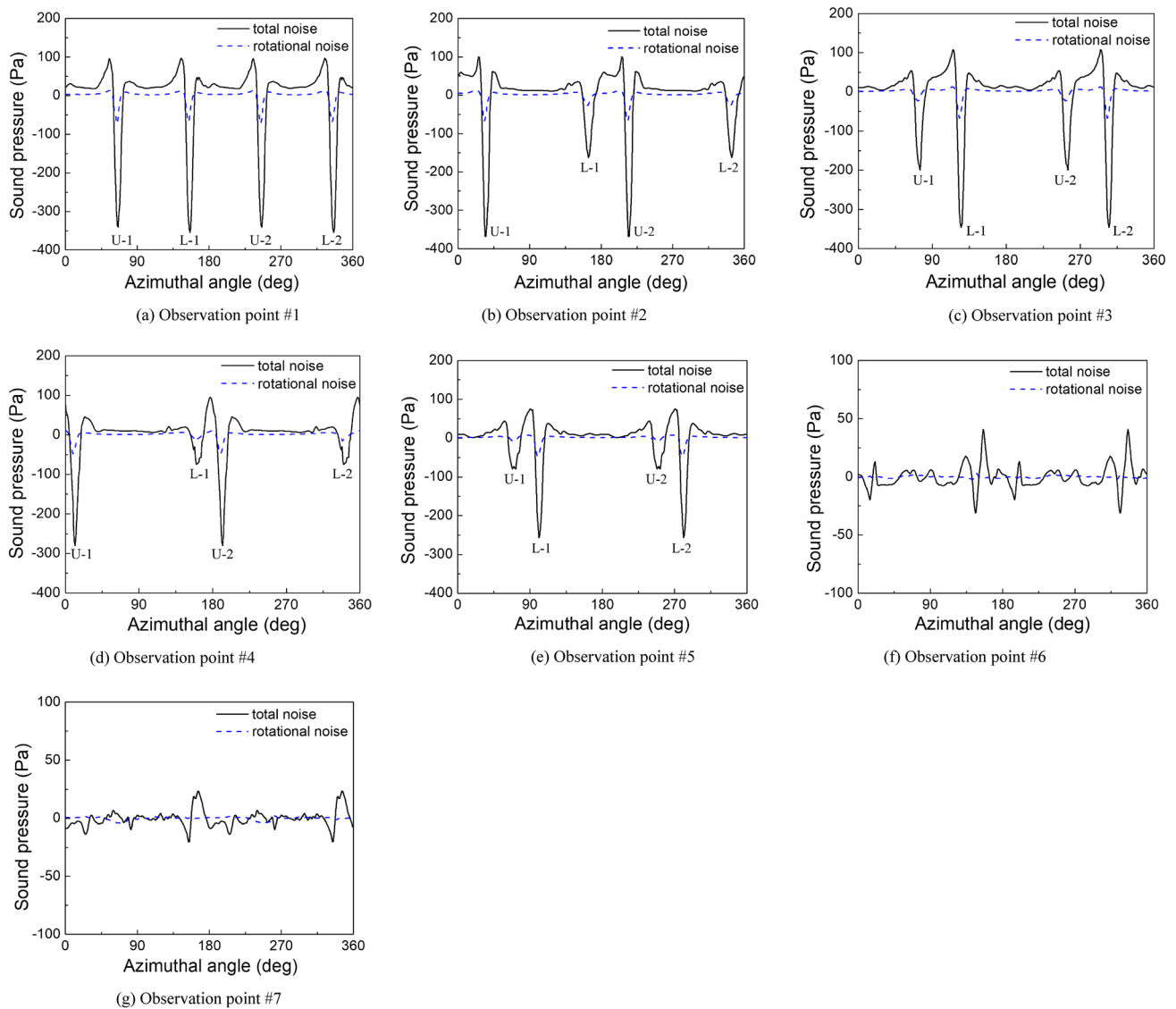


Fig. 18 Sound pressure time history of total noise and rotational noise in forward flight

the rear of the disk are far smaller than those in front of the rotor. In summary, in terms of the upper rotor or the lower rotor alone, the noise radiation intensity is the greatest at the observation points which are located in front of the rotor at the advancing side. However, in terms of the coaxial rotor, the sound pressure levels of the upper and lower rotors at the symmetrical observation points along the direction of forward flight are approximately the same in size, causing the noise radiation intensity of the coaxial rotor on both sides along the forward direction appears approximate a symmetrical distribution. This is one of the important differences in the characteristics of aerodynamic noise propagation between the coaxial rotor and the single rotor. The noise radiation intensity at the front of the rotor

still far exceeds that of the rear; this phenomenon is the same as the characteristics of the single rotor. Figure 19b shows that the sound pressure levels above and below the rotor exhibit an approximately symmetrical distribution, and the sound pressure levels directly in front of the rotor are far greater than those at the observation points above and below the rotor; these results are consistent with the characteristics of HSI noise propagation.

Figure 20 shows the sound pressure levels on the semi-spherical surface below the rotor, and the distance between observation points and the center of rotation is $5R$. The total noise sound pressure of the upper, the lower, and the coaxial rotor at various azimuth angles in the rotor disk plane are compared. The sound pressure levels on the semi-spherical

Fig. 19 Noise directivity patterns of the coaxial rotor

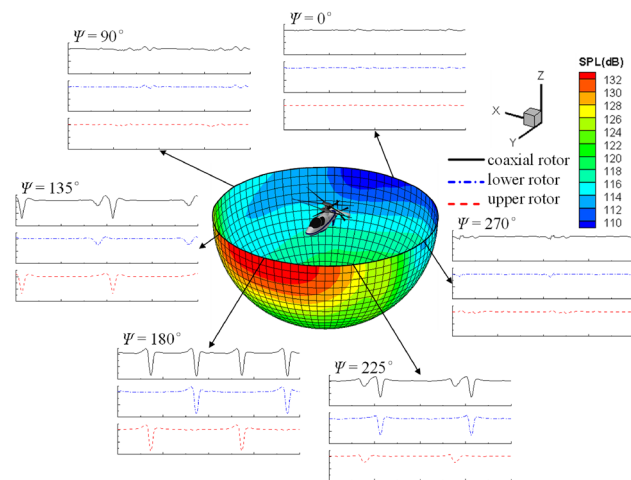
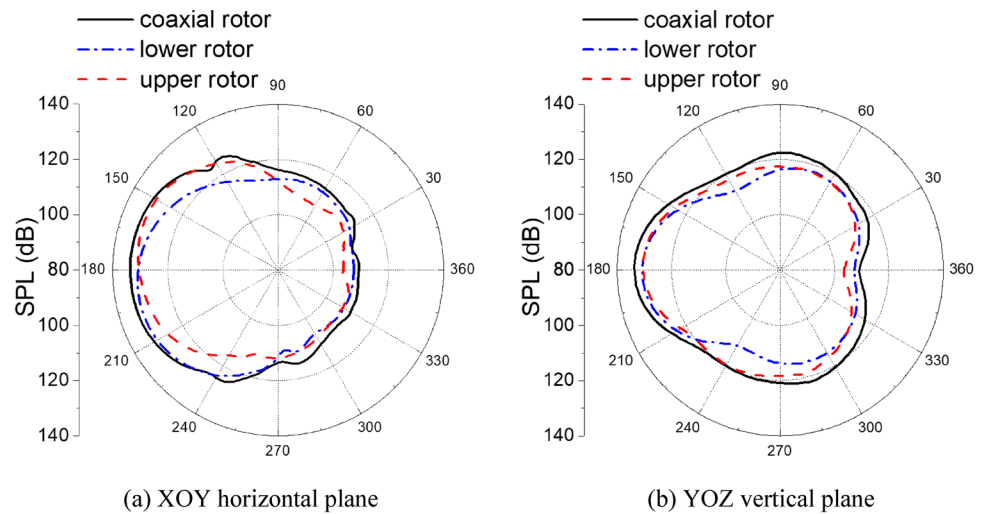


Fig. 20 Sound pressure levels on the semi-spherical surface below the coaxial rotor

surface below the rotor more intuitively reflects the noise pollution situation in varied directions in high-speed forward flight, which can help relevant personnel avoid the regions with the most severe helicopter noise pollution.

5 Conclusions

A method suitable for evaluating the aerodynamic noise of the coaxial rotor based on the CFD/FW–H method was established in this study to make an analysis of the aerodynamic noise characteristics of the coaxial rotor in hovering and forward flight. From the analysis of the calculation results, some conclusions can be obtained as follows:

1. There is a significant difference in the sound pressure waveform of the coaxial rotor at observation points in

different directions. In terms of the conventional single rotor, although the appearance time of negative peak values at varied observation points are different, the phase difference between adjacent peak values is the same. However, in terms of the coaxial rotor, at varied observation points, the different rotation directions of the upper and lower rotors cause greater differences to arise in the size of the peaks and phase difference between peaks. And, the phase difference between sound pressure waveforms of the upper and lower rotors is determined by the included angle of that observation point with the location where the upper and lower blades meet.

2. In the hovering state, the sound pressure peak values of thickness noise of the upper and lower rotors are approximately the same, however, significant differences exist in the sound pressure peak values of the loading noise of the two rotors. Compared with the gentle waveform of the thickness noise, the signal fluctuations of the loading sound pressure are more severe. The severe aerodynamic interference caused by the blade-tip vortex and the downwash of the upper rotor on the blade of the lower rotor leads to periodic changes in the loading of the lower rotor surface. In terms of the upper rotor, the thickness effect causes the surface loading of the upper rotor blade to show significant unsteady characteristics, increasing the radiation intensity of the loading noise. The loading noise of the upper rotor is generally greater than that of the lower rotor. Under the same thrust, the radiation intensity for the loading noise of a coaxial rotor is significantly stronger than that of a conventional single rotor.
3. During high-speed forward flight, in terms of the upper rotor or the lower rotor alone, the noise radiation intensity is the greatest at the observation points which are located in front of the rotor at the advancing side. The sound pressure levels of the upper and lower rotors at

the symmetrical observation points along the direction of forward flight are approximately the same. Because of the opposite rotation directions of the upper and lower rotors, the noise radiation intensity of the coaxial rotor on both sides along the forward direction exhibits an approximately symmetrical distribution, which is one of the important differences in the characteristics of aerodynamic noise propagation between the coaxial rotor and the single rotor. The noise radiation intensity directly in the front of the rotor is still far greater than the observation points at the rear of, above, and below the rotor, which is consistent with the characteristics of HSI noise propagation.

Acknowledgements This research is supported by the National Natural Science Foundation of China (No.11872211, No.12032012). Besides, this research is A Project Funded by the Priority Academic Program Development of Jiangsu Higher Education Institutions (PAPD).

Declarations

Conflict of interest The authors declare that there is no conflict of interest.

References

1. Leishman JG, Syal M (2008) Figure of merit definition for coaxial rotors. *J Am Helicopter Soc* 53:290–300
2. Andrew M (1980) Co-axial rotor aerodynamics in hover
3. Bagai A, Leishman JG (1996) Free-wake analysis of tandem, tilt-rotor and coaxial rotor configurations. *J Am Helicopter Soc* 41:196–207
4. Kim HW, Brown RE (2010) A rational approach to comparing the performance of coaxial and conventional rotors. *J Am Helicopter Soc* 55:12003
5. Tong Z, Mao S (1998) Navier stokes calculations of coaxial rotor aerodynamics. *Acta Aeronaut Et Astronaut Sin*
6. Lakshminarayan VK, Baeder JD (2010) Computational investigation of microscale coaxial-rotor aerodynamics in hover. *J Aircr* 47:940–955
7. Xu HY, Ye ZY (2010) Coaxial rotor helicopter in hover based on unstructured dynamic overset grids. *J Aircr* 47:1820–1824
8. Ye L, Xu GH (2012) Calculation on flow field and aerodynamic force of coaxial rotors in hover with CFD method. *Acta Aerodyn Sin* 30:437–442
9. Wachspress DA, Quackenbush TR (2006) Impact of rotor design on coaxial rotor performance, wake geometry and noise, annual forum proceedings-american helicopter society, American Helicopter Society, Inc, pp. 41
10. Kim HW, Duraisamy K, Brown R (2009) Effect of rotor stiffness and lift offset on the aeroacoustics of a coaxial rotor in level flight, 65th American Helicopter Society Annual Forum
11. Kim HW, Kenyon AR, Brown RE, Duraisamy K (2009) Interactional aerodynamics and acoustics of a hingeless coaxial helicopter with an auxiliary propeller in forward flight. *Aeronaut J* 113:65–78
12. Jia Z, Lee S (2019) Impulsive loading noise of a lift-offset coaxial rotor in high-speed forward flight. *AIAA J* 58:1–15
13. Jia ZH, Lee S, Sharma K, Brentner KS (2019) Aeroacoustic analysis of a lift-offset coaxial rotor using high-fidelity CFD/CSD loose coupling simulation
14. Zhao Q, Zhao G, Wang B, Wang Q, Shi Y, Xu G (2018) Robust Navier-Stokes method for predicting unsteady flowfield and aerodynamic characteristics of helicopter rotor. *Chin J Aeronaut* 31:214–224
15. Spalart P, Allmaras S (1992) A one-equation turbulence model for aerodynamic flows, 30th aerospace sciences meeting and exhibit, pp. 439
16. Yoon S, Jameson A (1988) Lower-upper symmetric-Gauss-Seidel method for the Euler and Navier-Stokes equations. *AIAA J* 26:1025–1026
17. Wang B, Zhao QJ, Xu G, Xu GH (2012) A new moving-embedded grid method for numerical simulation of unsteady flow-field of the helicopter rotor in forward flight. *Acta Aerodyn Sin* 30:14–21
18. Wang B, Yuan X, Zhao QJ, Zhu Z (2020) Geometry design of coaxial rigid rotor in high-speed forward flight. *Int J Aerosp Eng*. <https://doi.org/10.1155/2020/6650375>
19. Farassat (1981) Linear acoustic formulas for calculation of rotating blade noise. *Aiaa J* 19:1122–1130
20. Franciscantonio PD (1997) A new boundary integral formulation for the prediction of sound radiation. *J Sound Vib* 202:491–509
21. Coleman CP (1997) A survey of theoretical and experimental coaxial rotor aerodynamic research
22. Boxwell D, Schmitz F, Spletstoesser W, Schultz K (1987) Helicopter model rotor-blade vortex interaction impulsive noise: scalability and parametric variations. *J Am Helicopter Soc* 32:3–12
23. Spletstoesser W, Schultz K, Schmitz F, Boxwell D (1983) Model rotor high-speed impulsive noise-Parametric variations and full-scale comparisons, ahs
24. Li D, Yang Y (2011) Analysis on thickness noise generated from helicopter rotor with uneven blade spacing. *Acta Acust* 36:513–519

Publisher's Note Springer Nature remains neutral with regard to jurisdictional claims in published maps and institutional affiliations.